Energy Management and Control for Grid Connected Hybrid Energy Storage System under Different Operating Modes

Ujjal Manandhar, *Student Member*, IEEE, Abhisek Ukil, *Senior Member*, IEEE, Gooi Hoay Beng, *Senior Member*, IEEE, Narsa Reddy Tummuru, *Member*, IEEE, Sathish Kumar Kollimalla, *Member*, IEEE, Benfei Wang and Kalpesh Chaudhari, *Student Member*, IEEE

***Abstract*—DC-coupled microgrids are simple as they do not require any synchronization when integrating different distributed energy generations. However, the control and energy management strategy between the renewable energy sources and the energy storages under different operating modes is a challenging task. In this paper, a new energy management scheme is proposed for the grid connected hybrid energy storage with the battery and the supercapacitor under different operating modes. The main advantages of the proposed energy management scheme are effective power sharing between the different energy storage systems, faster DC link voltage regulation to generation and load disturbances, dynamic power sharing between the battery and the grid based on the battery state of charge, reduced rate of charge/discharge of battery current during steady state and transient power fluctuations, improved power quality features in AC grid and seamless mode transitions. The effectiveness of the proposed method is validated by both simulation and experimental studies.**

***Index Terms*—Battery, energy management, HESS, DC-coupled hybrid microgrid, supercapacitor.**

I. Introduction

The penetration of the distributed renewable generations like the photovoltaic (PV) and wind in the distribution network has been growing day by day. The PV generation is easily affected by the various environmental conditions. One of the primary countermeasure to solve the intermittent nature of the renewable power generations is to deploy the energy storage system [1]. The battery energy storages are generally used for PV and wind power system. The battery energy storages can deal with the slow power demand. However, it is unable to deal with high power fluctuation and may suffer from ageing problem when stressed to high frequency transient power fluctuations [2]–[4]. The ragone chart for different energy storages with their energy and power densities are presented in Fig. 1.

To deal with the above problem, combinations of energy storages with different characteristics are used. One of the popular combination is of the battery and supercapacitor (SC) system. The performance parameters of the battery and SC are summarized in Table I. The battery energy storages are employed to deal with the slow changing power demand while the SCs deal with the transient power fluctuations. The battery and SC combined hybrid energy storage system (HESS) is popular in renewable distributed generation systems [5]–[9], uninterruptible power supply applications [10], and in the hybrid electrical vehicle (EV) applications [11]–[13]. The battery and SC based HESS can effectively and efficiently solve the problem of varying power generation and load demand. To extend the life span of battery and SC, they shouldn't be overcharged/overdischarged. To maintain the energy storages in the safe operating region, the energy management scheme (EMS) is imperative, which can effectively utilize the energy storages and also protect them from overcharge/overdischarge problem.

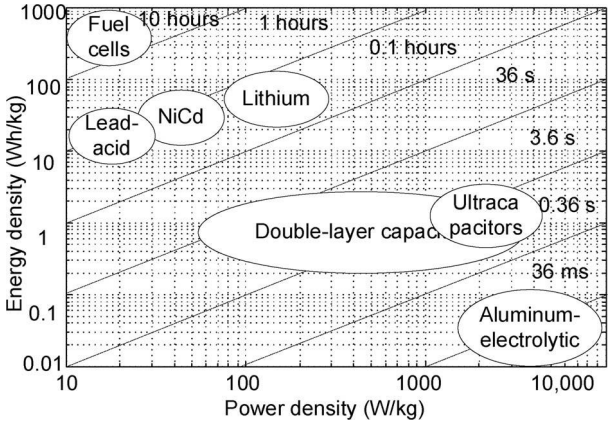

Fig. 1. Ragone chart for different energy storages with their power and energy densities [3].

TABLE I
Performance parameters for battery and supercapacitor [4]

	Lead-acid battery	Supercapacitor
Specific energy density	10-100(Wh/kg)	1-10(W/kg)
Specific power density	$<$ 1000(W/kg)	$<$ 10000(W/kg)
Cycle life	1000	$>$ 500000
Charge/discharge efficiency	70-85%	85-98%
Fast charge time	1-5hr	0.3-30s
Discharge time	0.3-3hr	0.3-30s

A. Literature Review

In [14], multi-mode fuzzy logic based power allocator for HESS is proposed. The solution provided in the paper solves the issues in haar wavelet method. In haar wavelet method, impacts of the state of charge (SOC) are generally neglected. But the practical application of the multi-mode fuzzy logic method is still a challenge. Adaptive fuzzy logic based EMS for HESS in EV application is discussed in [11]. The proposed control scheme uses the multi-agent based approach which is complex to design and requires large computational resources.

The fuzzy logic rule based control approach will generate the significant error between the simulated and experimental results as it is sensitive to the change in system parameters.

In [15], the adaptive neural network (ANN) based control for hyrbid AC/DC microgrid is presented. In the proposed method the ANN based control is applied to track the maximum power from the renewable source and to exchange power from the grid. The method is based on the online trained neural network controller which is too complex to modelled and requires large computational resources to get the optimal control parameters.

The model predictive control (MPC) based EMS and control for the HESS is presented in [16]. With the given control scheme, it is ensured that the battery and SC operate at predefined SOC limits. As the proposed approach is based on the classical discrete MPC, it requires large computational resources.

A unified EMS for grid-connected HESS is presented in [17]. The results presented show a better performance than the power management algorithm presented in [18], interms of faster DC voltage regulation, execution time and charge/discharge rates of the battery system. However, the power sharing between the grid and the battery during different operating conditions is based on the SOC level of the battery which follows a discrete pattern. This approach creates a sharp increase in the battery charge/discharge rates during transition which can reduce the battery operating lifetime [19].

In [7], [20] sliding mode control technique is used to control the HESS. The proposed methods are supported by detail experimental results. However, the control approach mentioned is complex to design and depend on system parameters. Various power management algorithms for grid connected system are presented in [21], [22]. The studies presented in these literatures follow the discrete power sharing approach between the battery and the grid. The low complexity power management and control strategy for isolated DC microgrid with HESS is presented in [23]. The energy management presented only deal with the isolated DC microgrid and neglect its connection with AC grid. In [24], a unified control and power management for PV-battery hybrid Microgrid for grid connected and islanding operation is presented. In the proposed method, battery balances the DC link and AC link power in all condition which increases the stress in the battery system. This will reduce the lifetime of the battery and also increase the system cost to meet the peak load demand. Xu *et. al* [25] proposed an extended droop control approach to obtain a decentralized power sharing between battery and SC during load and generation variations. The method is based on virtual resistance and virtual capacitance droop controller for reference power generation for battery and SC in DC microgird application.

B. Features of Proposed EMS and Control

To solve the aforementioned issues, a new EMS is presented in this paper. The features of the proposed EMS and control are: (i) faster DC link voltage restoration, (ii) operation of the battery and SC within their SOC limits, (iii) introduction of a new sharing coefficient for effective power sharing between the battery and the grid which reduces the rate of charge/discharge of the battery during long term operation and (iv) seamless mode transitions. The rest of the paper is organised as follows: The system architecture is described in Section II. The EMS is discussed in Section III. The simulation results are presented in Section IV. Experimental results and comparison between the existing methods are presented in Section V, followed by conclusion in Section VI.

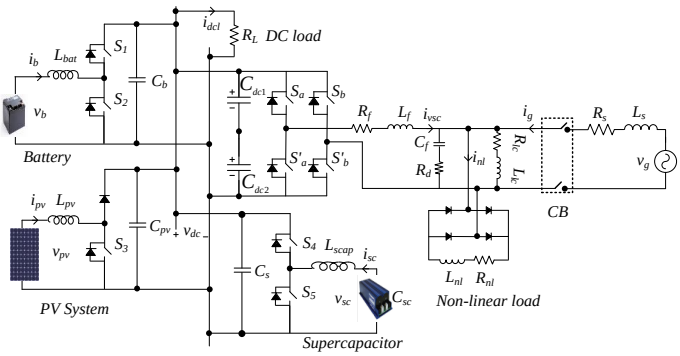

Fig. 2. Overall system architecture.

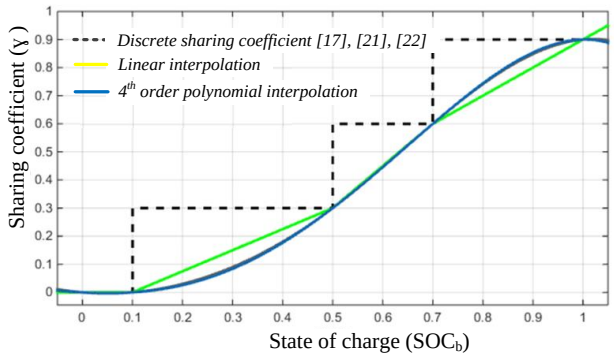

Fig. 3. Sharing coefficient (γ) for the proposed energy management scheme for deficit power mode.

II. System Architecture

The overall system architecture studied in this paper is shown in Fig. 2. It consists of emulated PV source, HESS and utility grid. The HESS is connected to the DC link with the half bridge bidirectional DC-DC converter which ensures the bidirectional power flow between the energy storage and the DC link. The DC link is connected to the AC grid with the voltage source converter which acts as a rectifier or an inverter depending upon the reference current. In Fig. 2, v_{pv}, v_b, v_{sc}, v_g and v_{dc} are PV, battery, SC, AC grid terminal voltage and DC link voltage respectively. L_{pv}, L_{bat}, L_{scap}, L_f and L_s are converter filter inductors for the PV, battery, SC, inverter and grid. C_{pv}, C_b and C_s are the filter capacitances of PV, battery, SC converters. S_1, S_2, S_3, S_4, S_5, S_a, S'_a, S_b and S'_b are representation of the control switches used for DC-DC converters and DC-AC inverter. i_{pv}, i_b, i_{sc}, i_{dcl}, i_{vsc}, i_g and i_{nl} represent the PV, battery, SC, DC load, inverter, grid and non-linear load current respectively. The overall DC load is represented by resistance R_L.

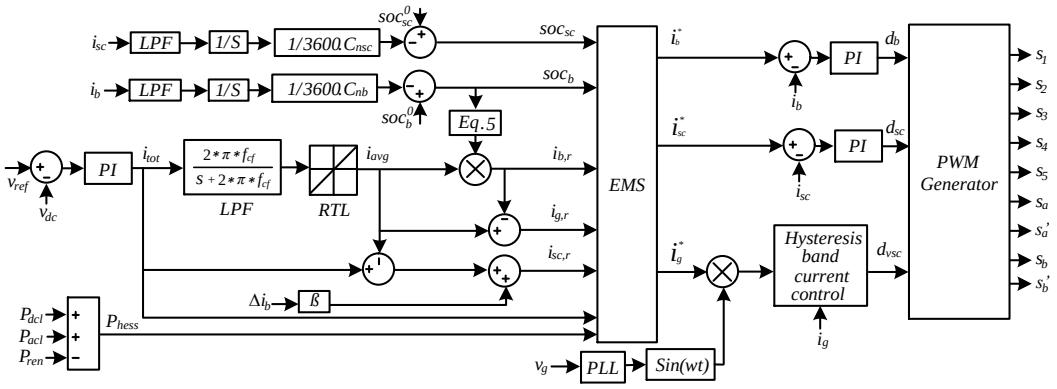

Fig. 4. Overall proposed unified control architecture.

III. EMS and Control Strategy

A. Reference Current Generation

The overall power balance should be maintained to make the system stable. The presented configuration and control scheme support the load in all operating conditions. Thus, the overall power balance equation to maintain a constant DC link voltage (v_{dc}) is as follows,

$$P_l(t) - P_{ren}(t) = P_b(t) + P_{sc}(t) + P_g(t) = P_{avg}(t) + \widehat{P}_{tran}(t), \quad (1)$$

where $P_{ren}(t)$, $P_b(t)$, $P_{sc}(t)$, $P_g(t)$ and $P_l(t)$ are the renewable energy source, battery, SC, grid and total load power respectively. $P_{avg}(t)$ and $\widehat{P}_{tran}(t)$ represents the total average power and transient power demand to be supplied/absorbed from the HESS and the utility grid to maintain the total power balance in the DC link. The DC link voltage is the reflection of the power balance among various sources and sinks [22]. Thus, The total current $i_{tot}(t)$ to be supplied or absorbed by HESS and grid is obtained from the voltage control loop and it is given in (2),

$$i_{tot}(t) = K_{pdc}\,(v_{ref} - v_{dc}) + K_{idc} \int (v_{ref} - v_{dc})\,dt, \quad (2)$$

where, K_{pdc} and K_{idc} are proportional and integral constant for the overall voltage loop proportional integral (PI) controller. In (2), v_{ref} is the reference DC link voltage. The effective sharing of DC current is essential to achieve a faster DC link voltage restoration and effective performance of the proposed control strategy. In conventional controller approach [18], low pass filter (LPF) is employed to extract an average component of the total effective current. The average current (i_{avg}) is given by (3),

$$i_{avg}(s) = \frac{2 * \pi * f_{cf}}{s + 2 * \pi * f_{cf}} i_{tot}(s), \quad (3)$$

$$i_{b,r}(s) = \gamma . i_{avg}(s),\ i_{g,r}(s) = (1 - \gamma) . i_{avg}(s), \quad (4)$$

where f_{cf}, $i_{b,r}(s)$, $i_{g,r}(s)$ and γ are the cut-off frequency of the LPF, the reference current for the battery converter control and the reference current for the grid and sharing coefficient. The cut-off frequency is chosen to be 5Hz as presented in [26]. Taking into account the voltage and SOC limit of the battery, it is important to select the appropriate sharing coefficient. As the i_{avg} is shared between the battery and the grid supply. The discrete power sharing approach is presented in the literature [17], [21], [22]. The discrete power sharing approach creates a sharp rate of change of battery current ($\frac{di_b}{dt}$) during sudden power fluctuation and during normal operation of charge/discharge when reaches to certain SOC limit of battery. The main objectives of the proposed sharing coefficient are to reduce the rate of change of battery current during normal operating condition and sudden power fluctuations and to maintain the SOC limit of battery for longer duration of time. The curve fitting technique from MATLAB is used to obtain a 4th order polynomial equation for sharing coefficient(γ).

$$\gamma = P_1 . (SOC_b)^4 + P_2 . (SOC_b)^3 + P_3 . (SOC_b)^2 + P_4 . SOC_b + P_5 \quad (5)$$

where, P_1 = -2.143, P_2 = 2.429, P_3 = 0.7071, P_4 = 0.09286, and P_5 = 1.832e-16. The graphical representation of the sharing coefficient is shown in Fig. 3. The transient and oscillatory component in the total reference current is given by (6),

$$i_{sc,r} = \widehat{i}_{tran}(s) = \left(1 - \frac{2 * \pi * f_{cf}}{s + 2 * \pi * f_{cf}}\right) i_{tot} + \beta \Delta i_b, \quad (6)$$

In (6), $i_{sc,r}$ and Δi_b are the SC reference current and the uncompensated current from the battery system. Here $\beta = \frac{v_b}{v_{sc}}$, is the compensation factor. The diversion of the uncompensated current from the battery system to SC system results in faster DC link voltage restoration. The generated battery, SC and grid reference currents are compared to the actual current. The i_b, i_{sc} and i_g are the actual battery, SC and grid current respectively. The error is then fed to the PI current control which generates a duty ratio to regulate the current. The rate limiter (RTL) is used with LPF to maintain the rate of charge/discharge of the battery below its maximum value [19]. The overall architecture of the proposed control and EMS is shown in Fig. 4.

B. Proposed EMS

The flow chart of the proposed EMS is presented in Fig. 5. It consists of two different modes, (i) excess power mode (EPM) and (ii) deficit power mode (DPM). The two modes of operation are identified based on the renewable power generation

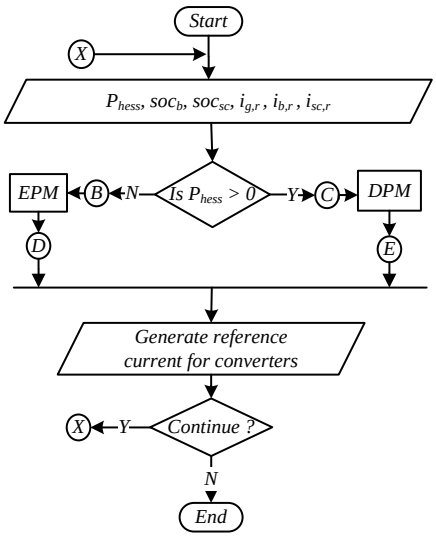

Fig. 5. Flowchart of the proposed EMS.

availability and the load demand in the system. They are deficit power mode ($P_{hess} > 0$) and excess power mode ($P_{hess} <= 0$) where $P_{hess} = P_b + P_{sc} + P_g = P_{dcl} + P_{acl} - P_{ren}$. Based on the condition of P_{hess} the system operates in different modes of operation as shown in flowchart Fig. 5. Under the DPM and EPM modes, four different operating conditions are identified based on the condition of SOC_b and SOC_{sc} as shown in Table II and Table III. The SOC_b and SOC_{sc} are the SOCs of battery and the SC respectively and calculated based on coulomb's counting method presented in [27].

$$SOC_b = SOC_b^0 - \frac{1}{3600.C_{nb}} \int i_b \, \mathrm{dt} \tag{7}$$

$$SOC_{sc} = SOC_{sc}^0 - \frac{1}{3600.C_{nsc}} \int i_{sc} \, \mathrm{dt} \tag{8}$$

where SOC_b^0, SOC_{sc}^0, C_{nb} and C_{nsc} are initial SOCs of battery and SC, nominal capacity of the battery and SC respectively. The proposed EMS meets the following objectives: (i) always maintains the SOC_b and SOC_{sc} within their safe operating region, i.e, higher (H) and lower (L) SOC limits as specified, (ii) limits the rate of charge/discharge of battery and SC, (iii) achieves seamless mode transition between different modes of operation, (iv) reduce stress on the battery and increase lifespan of the battery energy storage system, and (v) computationally less intense.

1) DPM: In this mode, the deficit power required to maintain the DC link voltage is supplied by the battery, grid and SC depending upon the SOC conditions of energy storage. In Table II, L_b and L_{sc} represent the lowest allowed SOC limits for battery and SC provided by the manufacturer. In the proposed scheme, the real power sharing between the grid and the battery system varies as in (5). The renewable power generation is operated at maximum power point in all four conditions in DPM. The various operations under the DPM are given in Table II and are explained below.

TABLE II
DPM

Conditions	Current setting
$SOC_b > L_b$ & $SOC_{sc} > L_{sc}$	$i_b^* = \gamma.i_{avg}, i_{sc}^* = i_{sc,r}$ $i_g^* = (1-\gamma).i_{avg}$
$SOC_b < L_b$ & $SOC_{sc} > L_{sc}$	$i_b^* = 0, i_{sc}^* = i_{sc,r}$ $i_g^* = i_{avg}$
$SOC_b > L_b$ & $SOC_{sc} < L_{sc}$	$i_b^* = \gamma.i_{avg}, i_{sc}^* = 0$ $i_g^* = (1-\gamma).i_{avg} + i_{sc,r}$
$SOC_b < L_b$ & $SOC_{sc} < L_{sc}$	$i_b^* = 0, i_{sc}^* = 0$ $i_g^* = i_{avg} + i_{sc,r}$

TABLE III
EPM

Conditions	Current setting
$SOC_b < H_b$ & $SOC_{sc} < H_{sc}$	$i_b^* = -i_{b,ra}, i_{sc}^* = -i_{sc,ra} + i_{sc,r}$ $i_g^* = i_{tot}$
$SOC_b > H_b$ & $SOC_{sc} < H_{sc}$	$i_b^* = 0, i_{sc}^* = -i_{sc,ra} + i_{sc,r}$ $i_g^* = i_{tot}$
$SOC_b < H_b$ & $SOC_{sc} > H_{sc}$	$i_b^* = -i_{b,ra}, i_{sc}^* = 0$ $i_g^* = i_{tot} + i_{sc,r}$
$SOC_b > H_b$ & $SOC_{sc} > H_{sc}$	$i_b^* = 0, i_{sc}^* = 0$ $i_g^* = i_{tot} + i_{sc,r}$

Condition I: If $SOC_b > L_b$ and $SOC_{sc} > L_{sc}$ then discharge both battery and SC. The current setting for the battery, SC and grid are as follows.

$$i_b^* = \gamma.i_{avg},\ i_{sc}^* = i_{sc,r},\ i_g^* = (1-\gamma).i_{avg} \tag{9}$$

The value of γ is changed dynamically based on the SOC_b value calculated based on (5).

Condition II: If $SOC_b < L_b$ and $SOC_{sc} > L_{sc}$ then the battery current is set to zero. The transient and oscillatory current is supplied by the SC and the average power demand is supplied by the grid. The current setting for the battery, SC and grid are as follows.

$$i_b^* = 0,\ i_{sc}^* = i_{sc,r},\ i_g^* = i_{avg} \tag{10}$$

Condition III: If $SOC_b > L_b$ and $SOC_{sc} < L_{sc}$ then the battery is discharged until SOC_b reach L_b to support the average power demand and the SC remains idle. The current setting for the battery, SC and grid are as follows.

$$i_b^* = \gamma.i_{avg},\ i_{sc}^* = 0,\ i_g^* = (1-\gamma).i_{avg} + i_{sc,r} \tag{11}$$

Condition IV: If $SOC_b < L_b$ and $SOC_{sc} < L_{sc}$ then both the battery and the SC remain idle. The grid supports the total power mismatch between the generation and load. The current setting for the battery, SC and grid are as follows.

$$i_b^* = 0,\ i_{sc}^* = 0,\ i_g^* = i_{avg} + i_{sc,r} \tag{12}$$

In this condition, the average power as well as transient power demand is supplied from the grid.

2) EPM: In this mode, the excess power from the renewable energy sources is stored into the battery and SC until SOC_b and SOC_{sc} reach their highest limits. In Table III, H_b and H_{sc} represent the highest safe operating SOC limit for battery and SC provided by the manufacturer. Once the ESS reaches its highest SOC limit, the excess energy is fed to the grid using DC-AC inverter. The operating conditions in EPM

TABLE IV
SYSTEM PARAMETERS FOR SIMULATION STUDY

PV array parameters @ STC	**Values**
Open circuit voltage (v_{pv})	40 V
Short circuit current (i_{pv})	20 A
Battery specifications	**Values**
Type	Lead Acid
Ah capacity	12 Ah
Terminal Voltage (v_b)	12 V
No of batteries in series	4
SC specifications	**Values**
Terminal voltage (v_{sc})	15V
Capacitance (C_{sc})	58F
No of SCs in series	4
Maximum continuous current	20A
Maximum current in $1sec$	80A
Converters parameters	L_{pv} = 10 mH, C_{pv} = 440 µF L_{bat} = 1.63 mH, C_b = 440 µF L_{scap} = 2 mH, C_s = 440 µF C_{dc1} = 1600 µF, C_{dc2} = 1600 µF L_f = 5mH, C_f = 15 µF L_s = 5mH
Controller parameters	k_{pv} = 0.1, k_{ipv} = 1 k_{pb} = 0.1, k_{ib} = 100 k_{psc} = 0.4, k_{isc} = 150 k_{pdc} = 1, k_{idc} = 100 β = 0.85
Load parameters	R_L = 50 Ω, R_{lc} = 20 Ω R_{nl} = 30Ω, L_{nl} = 50mH
DC and AC grid parameters	v_{dc} = 80V, v_g = 50V, 50Hz

are given in Table III. In Table III, $i_{b,ra}$ and $i_{sc,ra}$ are the battery and SC rated charging current.

IV. Simulation Results

The nominal system parameters used during simulation are listed in Table IV. In Table IV, k_{pv}, k_{pb}, k_{psc} are the proportional constants of PV, battery and SC current loop PI controller. k_{ipv}, k_{ib}, k_{isc} are the integral constants of PV, battery and SC current loop PI controller. The SOC_b and SOC_{sc} limits are varied intentionally to observe the extreme operation conditions in different operating modes during both simulation and experimental studies.

A. Performance under DPM Operation

The performance of the proposed EMS for DPM operation is shown in Fig. 6. In this mode, the PV generation is kept constant. SOC_b and SOC_{sc} limits are varied to study the behaviour of the system in extreme conditions. The purpose to do so is to study the behaviour of the controller and proposed energy management algorithm during extreme operating conditions.

At time t_1, SOC_b and SOC_{sc} are above lower SOC limit. At the same time instant, the DC load is changed from $R = 50\Omega$ to $R = 25\Omega$, which creates a voltage deviation in the DC link. In Fig. 6 (c) it can be observed that the SC responds to deal with the fast changing transient power demand and the battery current slowly increases.

At time t_2, SOC_b is decreased below L_b while the SOC_{sc} is still above L_{sc}. In this condition, the transient power is absorbed by the SC and the active power demand is dealt by the grid supply.

At time t_3, SOC_b is higher than L_b and SOC_{sc} is below L_{sc}. In this instant, the transient power is dealt by the grid

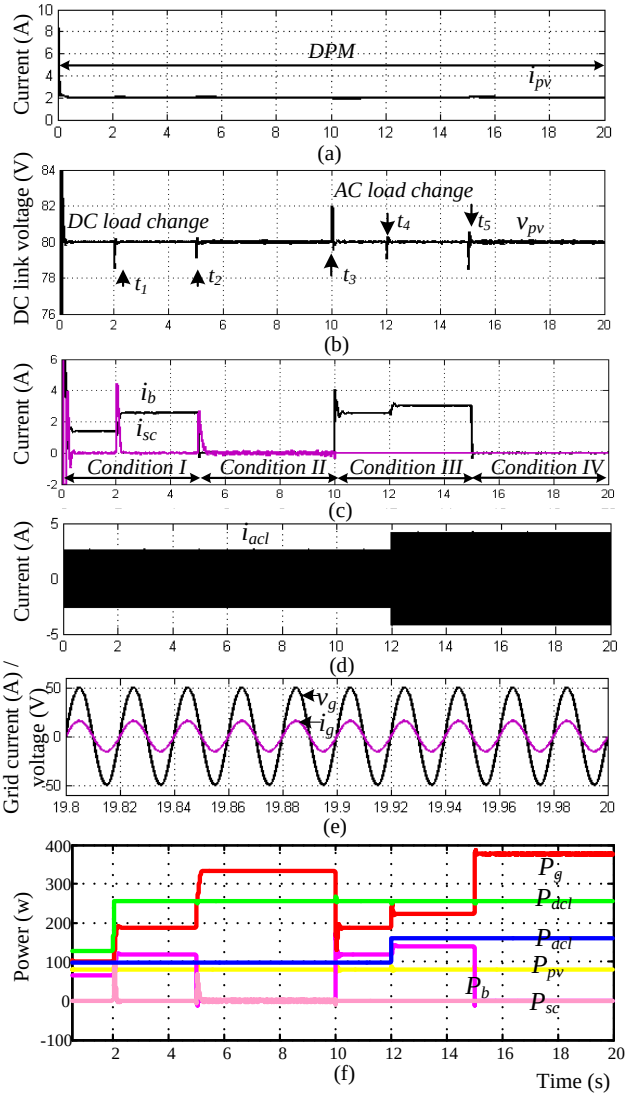

Fig. 6. Performance under DPM operation: (a) PV current, (b) DC link voltage, (c) SC and battery current, (d) AC load current,(e) grid current and voltage and (f) Powers.

supply and the average power is shared based on the sharing coefficient in (5).

At time t_4, the AC load is increased by decreasing the linear load resistance. At this time, SOC_{sc} is below L_{sc}. So, the i_{sc} is zero. The i_b slowly rises as the grid participates to compensate the deficit of SC in the system.

At time t_5, SOC_b is below L_b, and SOC_{sc} is below L_{sc}. In this condition, the grid supplies the required power to stabilise the DC link voltage. In this condition, if the grid is not available we should consider the load shedding control techniques to maintain the power balance in the system.

B. Performance under EPM Operation

The performance of the proposed EMS for EPM operation is shown in Fig. 7. In this mode the generation is made higher than the load demand. At time t_1, SOC_b and SOC_{sc} are below H. At time $t_1 = 2s$, the DC load is changed from $R = 50\Omega$ to $R = 25\Omega$, which creates a voltage deviation in the DC link. In this condition the battery and SC are charged with

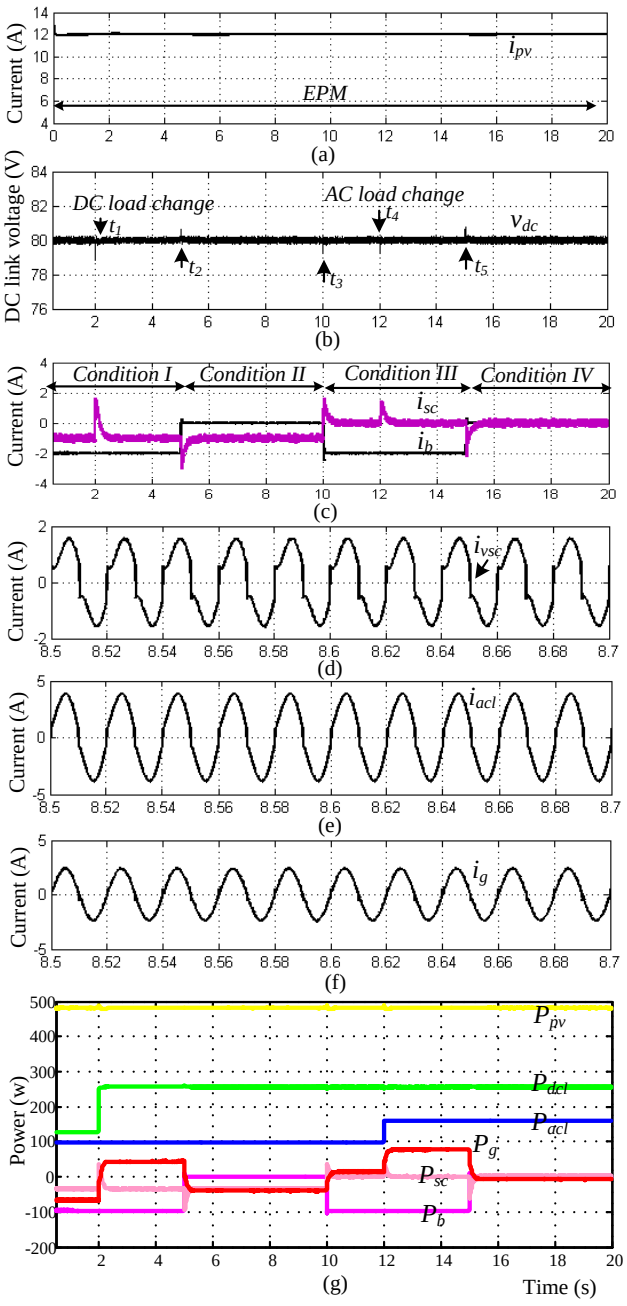

Fig. 7. Performance under EPM operation: (a) PV current, (b) DC link voltage, (c) SC and battery current, (d) inverter current, (e) AC load current,(f) grid current and (g) Powers.

their rated charging capacity until the highest SOC limit is achieved. The required average power to maintain the constant DC link voltage in this condition is maintained by the grid. The transient power is supplied by the SC system.

At time t_2, SOC_b reaches to H_b so the battery charging current is zero. In this condition the SC is charged with the rated charging current as the SOC_{SC} is still below H_{sc}. The remaining excess power is fed to the grid as shown in Fig. 7 (g). The grid power is negative from time t_2 to t_3, as the excess power is fed to the grid.

At time t_3, SOC_{sc} reaches to H_{sc} so that the SC charging current is zero. In this condition, the battery is charged with rated charging current until H_b is achieved. And the grid takes

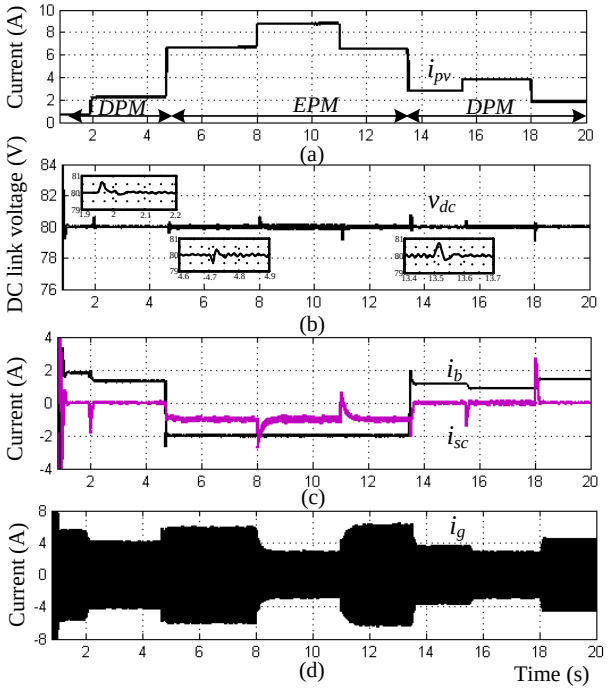

Fig. 8. Performance under change in various operating modes: (a) PV current, (b) DC link voltage, (c) SC and battery current and (d) grid current.

the transient and average power to maintain the constant DC link voltage.

At time instant t_4, the AC load is increased by decreasing the linear load resistance. During this time period, SOC_{sc} is at H_{sc} and SOC_b is below H_b. The i_b charging current remains unchanged while i_{sc} supplies the transient power demand.

At time t_5, SOC_b and SOC_{sc} are made above the H SOC limit. In this condition, the grid takes all the power to stabilise the DC voltage. All the load is supplied by the generation, and the excess power is fed to the grid. In all the operating conditions, the grid current and voltage are operating in unity power factor in all conditions. The inverter, AC load and grid currents are shown in Fig. 7 (d)-(f) respectively.

C. Seamless Mode Transition

The transition from one mode to another is shown in Fig. 8. The PV generation is changed by changing the reference current value for the PV converter control. During this study, the SOC_b and SOC_{sc} are maintained between L and H. The transient power is controlled by the SC system as shown in the Fig. 8 (c) and slow changing power demand is shared by the grid current and the battery system as shown in the Fig. 8 (c) and Fig. 8 (d). The smooth restoration of the DC link voltage is observed in all operating conditions with varying PV generation.

V. Experimental Results

The hardware prototype for a grid connected DC microgrid with HESS is built, as shown in Fig. 9. The Semikron SKM 75GB12T4 control switches are used to build DC-DC converters and a single phase DC-AC inverter. The LEM current

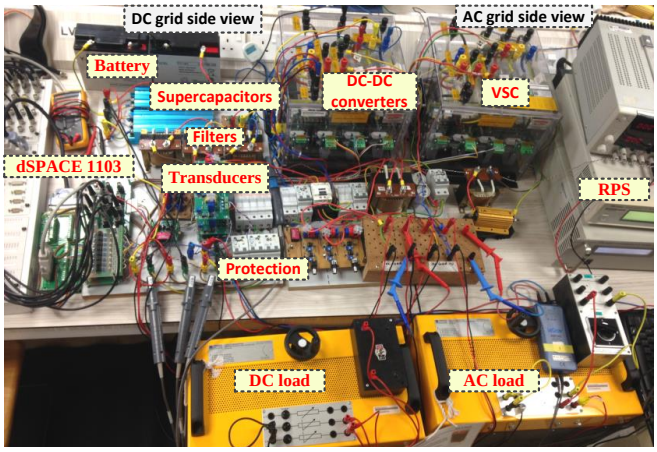

Fig. 9. Hardware setup.

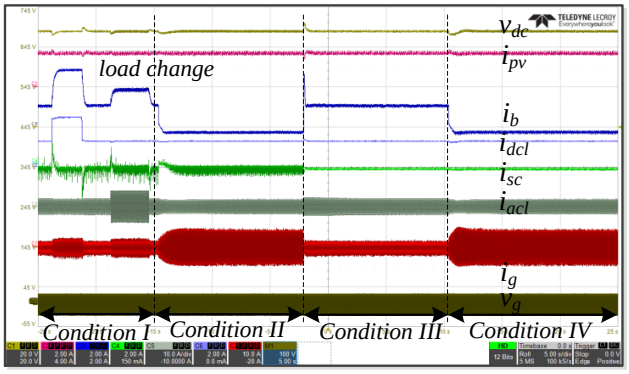

Fig. 10. Experimental result for DPM operation. $v_{dc} \sim$ 20V/div, i_{pv}, i_b, i_{sc}, $i_{dcl} \sim$ 2A/div, i_g, $i_{acl} \sim$ 10A/div, $v_g \sim$ 100V/div, $time \sim$ 5s/div.

and voltage transducers are used to measure the currents and the voltages. The chroma programmable DC power supply 62012P-600-8 is used as a renewable power source (RPS) in the experiment. The RPS is connected to the DC link using a DC-DC boost converter. The current from the RPS is controlled by changing the reference current for the DC-DC boost converter current controller. The different current references are fed to the current controller to generate different PV current profiles during the experimental study. The two series combinations of 17Ah capacity lead acid battery with terminal voltage of 12V are used as a battery system. The two series combinations of Maxwell BMOD0058 E015 B01 SC with capacity of 58F at 15V are used as a SC system. The maximum discharge current for SC in 1sec is 80A. The dSPACE 1103 real-time controller is used as a control platfrom. The DC link voltage (v_{dc} = 48V) and AC grid voltage (v_{ac} = 20V (rms)) are chosen for the experimental study. It is highlight that the experimental setup is the scaled down version of the system used during the simulation study.

A. Performance under Different Modes of Operation

The experimental results for the DPM and EPM operations are shown in Fig. 10 and Fig. 11 respectively.

The possible operating conditions during the DPM are shown in Fig. 10. The average deficit power is shared between

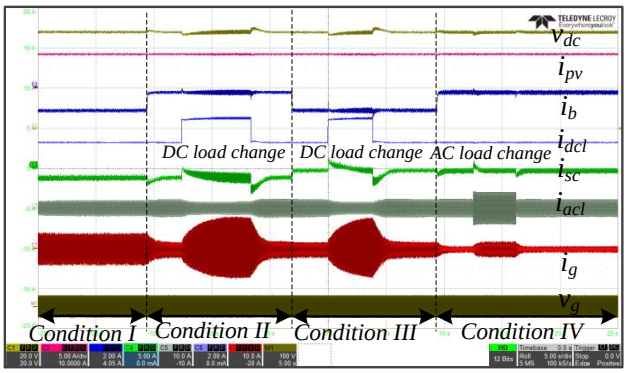

Fig. 11. Experimental result for EPM operation. $v_{dc} \sim$ 20V/div, i_{pv}, $i_{sc} \sim$ 5A/div, i_b, $i_{dcl} \sim$ 2A/div, i_g,$i_{acl} \sim$ 10A/div, $v_g \sim$ 100V/div, $time \sim$ 5s/div.

the grid and the battery according to the sharing coefficient mentioned in (5). This approach reduces stress in the battery, as the sharing coefficient varies with respect to SOC_b. The four conditions are analysed where SOC_b and SOC_{sc} limits are changed intentionally to observe the extreme conditions. It is observed that the energy storages participate to maintain the system balance until their SOC limit is less than their lower SOC limit in DPM.

In Fig. 11, four operating conditions during EPM are studied. In condition I, the battery and SC are charged with the excess power with its rated charging current ($i_{b,ra}$ and $i_{sc,ra}$) until H_b and H_{sc} are achieved. In this case, the DC link is maintained by the grid power supply. In condition II, the battery charging current is set to zero as SOC_b reaches to H_b. In condition III, i_{sc} is zero as SOC_{sc} reaches the H_{sc}. The soft change in the grid current is observed during transition and load change as SC supports the transient power demand. In condition IV, i_b and i_{sc} are made zero as they reached their maximum storage limits and the excess power is fed to the grid. During the load change conditions in different modes, the transient power is supported by SC and average power is shared between battery and grid.

B. Long-term Performance Analysis

Fig. 12 illustrates the operation of proposed controller under a general operational case when the PV generation changes in random manners. The PV irradiation data is recorded every one minute from 10:00 am to 16:30 pm. The irradiation pattern obtained is shown in Fig. 12 (a). In this experiment, SOC_b and SOC_{sc} are maintained under safe operating regions.

The respective i_{pv} pattern is generated as per the irradiation pattern, shown in Fig. 12 (b). It is observed from the experiment that the proposed controller is effective in managing the intermittent PV power (represented by i_{pv}), by effectively controlling the slow base power fluctuations from the battery (represented by i_b), and the faster transient power fluctuations from the SC system. The DC link voltage is maintained at the constant value.

The AC grid voltage and current through grid are in phase. The DC-AC inverter compensates the harmonics components for the non-linear part of the AC load. Thus, the grid voltage and current are operated at unity power factor. In Fig. 12 (b), the step change in the DC load is done at time t_1 and t_2 along

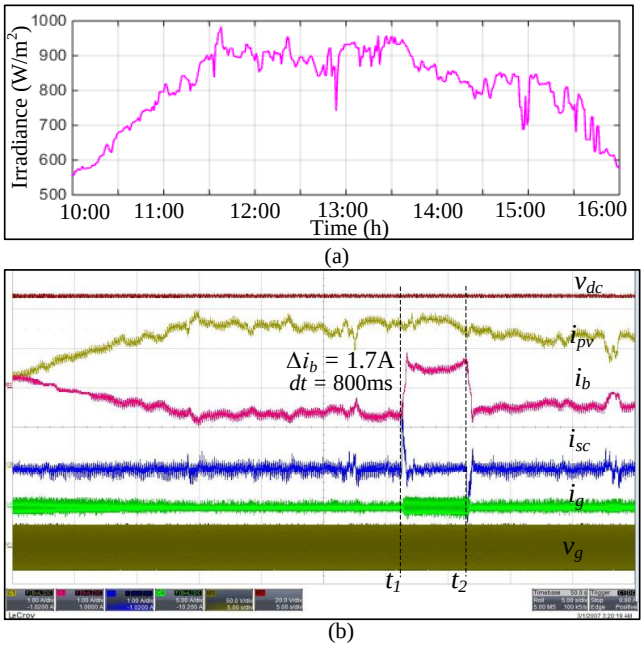

Fig. 12. Experimental result for long-term PV change. (a) Irradiance pattern from 10:00 am - 16:30 pm. (b) $v_{dc} \sim$ 20V/div, i_{pv}, i_b, $i_{sc} \sim$ 1A/div, $i_g \sim$ 5A/div, $v_g \sim$ 50V/div, $time \sim$ 5s/div.

with PV generation variation. At time t_1, the battery changes its modes from charging current of $-0.8A$ to discharging current of $0.9A$ to meet the varying load demand. During the step change in load demand the SC absorbs the transient power due to load as well as variation due to PV which reduces the stress in the battery system. The battery current slowly increases to compensate the low frequency power demand. This ensures less stress in the battery system during the long-term operation and stable DC grid operation.

C. Short-term Performance Analysis

The operation of the conventional control strategy [17], [18] and proposed EMS during step change in load demand is presented in Fig. 13 (a) and (b) respectively. v_{dc}, v_{ac} are constant during the step increase and decrease in the load demand. i_b and i_g interact with each other to support the average power demand. The transient current fluctuation caused by the step load change is taken care by the SC system. During this condition, the grid operates at unity power factor. The $\frac{di_b}{dt}$ of the battery is maintained below its maximum rate of charge/discharge. The zoomed view of the the step decrease in load demand at point t_4 is shown in Fig. 13 (c). The results shows average power shared between the battery and grid. It is also observed that the grid current and voltage are in phase which ensures the unity power factor operation. The measured total harmonic distortion in the grid current in Fig. 13 (c) is less than 7%.

As shown in Fig. 13 (c), the SC system handles the transient current requirement during sudden load change and the high frequency switching current ripple from PV DC-DC converter and battery DC-DC converter. Thus a smooth DC link voltage is obtained in the system.

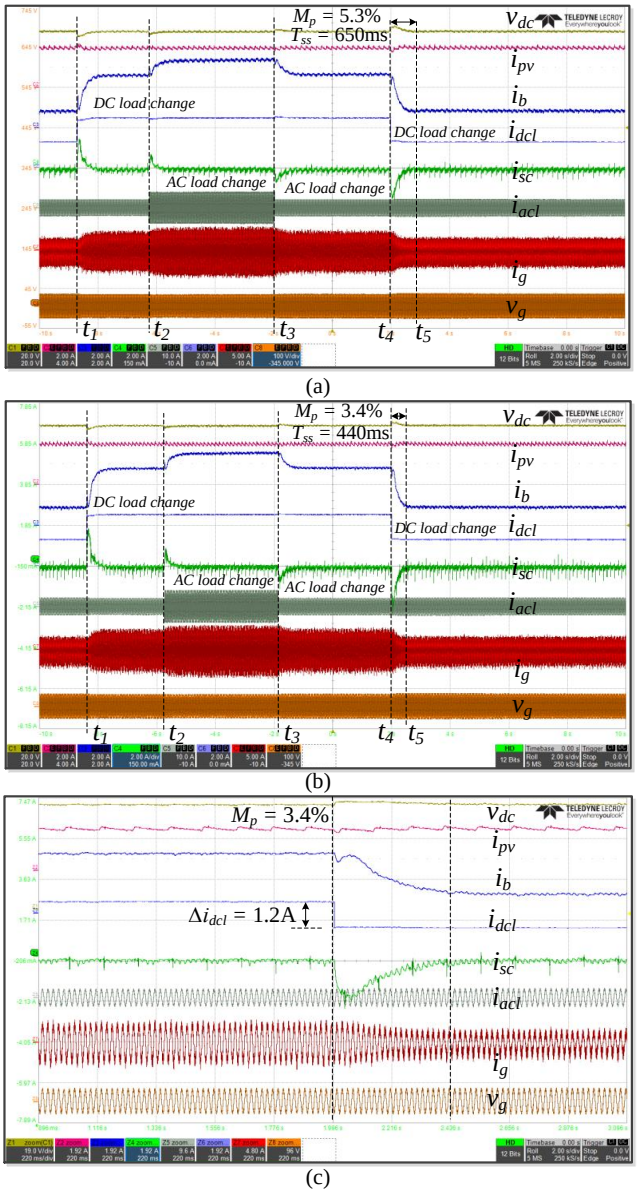

Fig. 13. Experimental result for step change in load demand. (a)Results for control scheme [17], [18]. (b) Results for proposed controller. (c) zoomed view of Fig. 12 (b) at point t_4. $v_{dc} \sim$ 20V/div, i_{pv}, i_b, i_{sc}, $i_{dcl} \sim$ 2A/div, $i_{acl} \sim$ 10A/div, $i_g \sim$ 5A/div, $v_g \sim$ 100V/div, $time \sim$ 2s/div.

TABLE V
PERFORMANCE COMPARISONS WITH VARIOUS CONTROL SCHEMES

Performance index	[16]	[17], [18]	Proposed
Peak overshoot (M_p)	-	5.3%	3.4%
Settling time (T_{ss})	-	650ms	440ms
$\frac{di_b}{dt}$ ratio (A/s)	-	0.8	0.05
Execution time (T_s)	0.01s	75μs	30μs

D. Performance Comparison of Proposed Controller with the Existing Method

Fig. 14 shows the comparison of the performance of the proposed controller with the existing methods [17], [18], for smoothing the battery power fluctuations. In the experiment the SOC_b is changed as shown in the Fig. 14 (a). As the control schemes in [17], [18] follow the discrete pattern to

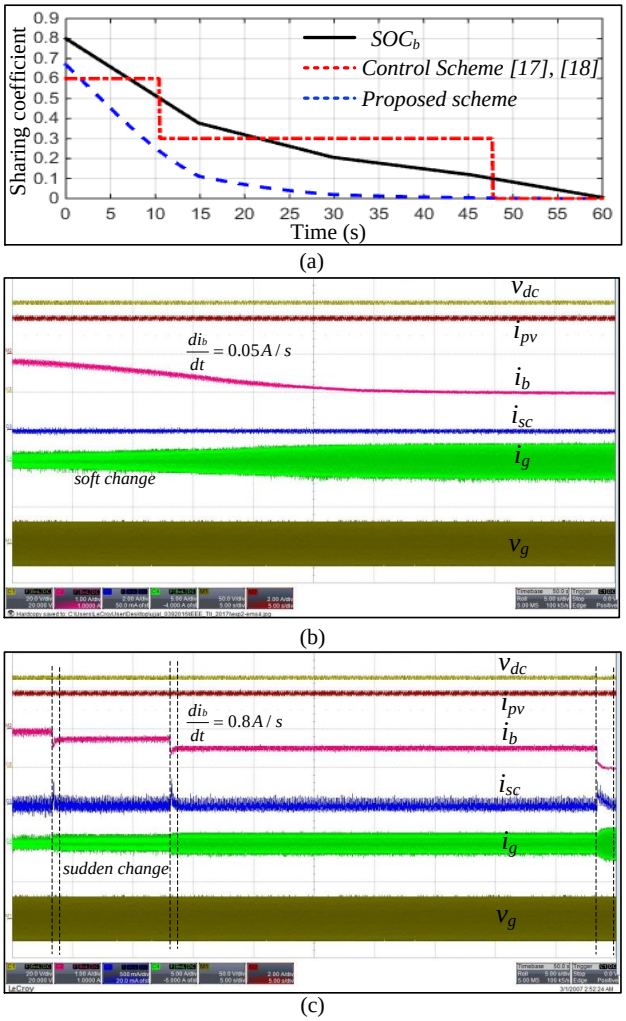

Fig. 14. Experimental result for dynamic SOC_b change. (a) SOC_b change and sharing coefficient. (b) Results for proposed controller and (c) Results for control scheme [17], [18]. $v_{dc} \sim$ 20V/div, $i_{pv} \sim$ 2A/div, $i_b \sim$ 1A/div, $i_{sc} \sim$ 0.5A/div, $i_g \sim$ 5A/div, $time \sim$ 5s/div.

change the current sharing reference, the sharp changes in the battery current are observed in Fig. 14 (c). Taking into account the voltage and SOC limit, it is important to select the appropriate smoothing sharing coefficient. The battery reference current is varied dynamically in the proposed scheme, so the $\frac{di_b}{dt}$ for proposed method is lower compared to the existing methods [17], [18]. The grid provides more power in the proposed control to reduce stress in the battery from large average power demand. Thus, in Fig. 14 (b), the current from the grid is higher compared to the Fig. 14 (c) at the same time instants.

The voltage overshoot ($M_p = \frac{\Delta v_{dc}}{v_{dc}} * 100\%$) and settling time ($T_{ss}$) during step decrease in load demand is studied based on the experimental results shown in Fig. 13 (a) and (b) at time t_4. The rate of change of the battery current $\frac{di_b}{dt}$ is compared based on the experimental result presented in Fig. 14. The comparisons are presented in Table V. The result obtained shows the better performance of the proposed controller in terms of faster DC link voltage restoration with less peak overshoot during step change in load demand.

VI. Conclusion

The new energy management scheme and control for grid connected HESS are presented in this paper. The main features of the proposed energy management scheme are less stress in the battery system, dynamic power sharing between the battery and grid, faster DC link voltage restoration and maintain the SOC limits of energy storage within the safe operating region. The proposed energy management scheme and control is effective in seamless mode transition between various modes of operation. The performance of the proposed control approach to reduce the stress in the battery during the normal operation and sudden changes in load and generation is also studied. The effectiveness of the proposed controller over the existing controller is also presented in the paper.

References

[1] C. Wang, X. Yang, Z. Wu, Y. Che, L. Guo, S. Zhang, and Y. Liu, "A highly integrated and reconfigurable microgrid testbed with hybrid distributed energy sources," *IEEE Trans. Smart. Grid*, vol. 7, no. 1, pp. 451–459, Jan. 2016.

[2] J. Xiao, P. Wang, and L. Setyawan, "Multilevel energy management system for hybridization of energy storages in dc microgrids," *IEEE Trans. Smart. Grid*, vol. 7, no. 2, pp. 847–856, Mar. 2016.

[3] H. Zhou, T. Bhattacharya, D. Tran, T. S. T. Siew, and A. M. Khambadkone, "Composite energy storage system involving battery and ultracapacitor with dynamic energy management in microgrid applications," *IEEE Trans. Power. Electron.*, vol. 26, no. 3, pp. 923–930, Mar. 2011.

[4] M. E. Glavin, P. K. W. Chan, S. Armstrong, and W. G. Hurley, "A standalone photovoltaic supercapacitor battery hybrid energy storage system," in *13th International Power Electron. and Motion Control Conf.*, Sept. 2008, pp. 1688–1695.

[5] J. Pegueroles-Queralt, F. D. Bianchi, and O. Gomis-Bellmunt, "A power smoothing system based on supercapacitors for renewable distributed generation," *IEEE Trans. Ind. Electron.*, vol. 62, no. 1, pp. 343–350, Jan. 2015.

[6] B. Hredzak, V. G. Agelidis, and G. D. Demetriades, "A low complexity control system for a hybrid dc power source based on ultracapacitor," *IEEE Trans. Power. Electron.*, vol. 29, no. 6, pp. 2882–2891, Jun. 2014.

[7] D. B. W. Abeywardana, B. Hredzak, and V. G. Agelidis, "A fixed-frequency sliding mode controller for a boost-inverter-based battery-supercapacitor hybrid energy storage system," *IEEE Trans. Power. Electron.*, vol. 32, no. 1, pp. 668–680, Jan. 2017.

[8] B. V. Solanki, K. Bhattacharya, and C. A. Caizares, "A sustainable energy management system for isolated microgrids," *IEEE Trans. Sust. Ene.*, vol. 8, no. 4, pp. 1507–1517, Oct. 2017.

[9] J. Tan and Y. Zhang, "Coordinated control strategy of a battery energy storage system to support a wind power plant providing multi-timescale frequency ancillary services," *IEEE Trans. Sust. Ene.*, vol. 8, no. 3, pp. 1140–1153, Jul. 2017.

[10] A. Lahyani, P. Venet, A. Guermazi, and A. Troudi, "Battery/supercapacitors combination in uninterruptible power supply (ups)," *IEEE Trans. Power. Electron.*, vol. 28, no. 4, pp. 1509–1522, Apr. 2013.

[11] H. Yin, W. Zhou, M. Li, C. Ma, and C. Zhao, "An adaptive fuzzy logic-based energy management strategy on battery/ultracapacitor hybrid electric vehicles," *IEEE Trans. Trans. Electri.*, vol. 2, no. 3, pp. 300–311, Sept. 2016.

[12] L. Sun, K. Feng, C. Chapman, and N. Zhang, "An adaptive power-split strategy for battery, supercapacitor powertrain, design, simulation, and experiment," *IEEE Trans. Power. Electron.*, vol. 32, no. 12, pp. 9364–9375, Dec. 2017.

[13] Z. Amjadi and S. S. Williamson, "Prototype design and controller implementation for a battery-ultracapacitor hybrid electric vehicle energy storage system," *IEEE Trans. Smart. Grid*, vol. 3, no. 1, pp. 332–340, Mar. 2012.

[14] X. Feng, H. B. Gooi, and S. X. Chen, "Hybrid energy storage with multimode fuzzy power allocator for pv systems," *IEEE Trans. Sust. Ene.*, vol. 5, no. 2, pp. 389–397, Apr. 2014.

[15] N. Chettibi, A. Mellit, G. Sulligoi, and A. M. Pavan, "Adaptive neural network-based control of a hybrid ac/dc microgrid," *IEEE Trans. Smart. Grid*, vol. PP, no. 99, pp. 1–13, 2016.

[16] B. Hredzak, V. G. Agelidis, and M. Jang, "A model predictive control system for a hybrid battery-ultracapacitor power source," *IEEE Trans. Power. Electron.*, vol. 29, no. 3, pp. 1469–1479, Mar. 2014.
[17] N. R. Tummuru, M. K. Mishra, and S. Srinivas, "Dynamic energy management of renewable grid integrated hybrid energy storage system," *IEEE Trans. Ind. Electron.*, vol. 62, no. 12, pp. 7728–7737, Dec. 2015.
[18] R. Sathishkumar, S. K. Kollimalla, and M. K. Mishra, "Dynamic energy management of micro grids using battery super capacitor combined storage," in *Annual IEEE India Conf. (INDICON)*, Dec. 2012, pp. 1078–1083.
[19] S. K. Kollimalla, A. Ukil, H. B. Gooi, U. Manandhar, and N. R. Tummuru, "Optimization of charge/discharge rates of a battery using a two-stage rate-limit control," *IEEE Trans. Sust. Ene.*, vol. 8, no. 2, pp. 516–529, Apr. 2017.
[20] B. Wang, J. Xu, R. J. Wai, and B. Cao, "Adaptive sliding-mode with hysteresis control strategy for simple multimode hybrid energy storage system in electric vehicles," *IEEE Trans. Ind. Electron.*, vol. 64, no. 2, pp. 1404–1414, Feb. 2017.
[21] S. Kotra and M. K. Mishra, "A supervisory power management system for a hybrid microgrid with hess," *IEEE Trans. Ind. Electron.*, vol. 64, no. 5, pp. 3640–3649, May. 2017.
[22] N. Korada and M. K. Mishra, "Grid adaptive power management strategy for an integrated microgrid with hybrid energy storage," *IEEE Trans. Ind. Electron.*, vol. 64, no. 4, pp. 2884–2892, Apr. 2017.
[23] S. K. Kollimalla, M. K. Mishra, A. Ukil, and H. B. Gooi, "Dc grid voltage regulation using new hess control strategy," *IEEE Trans. Sust. Ene.*, vol. 8, no. 2, pp. 772–781, Apr. 2017.
[24] Z. Yi, W. Dong, and A. H. Etemadi, "A unified control and power management scheme for pv-battery-based hybrid microgrids for both grid-connected and islanded modes," *IEEE Trans. Smart. Grid*, vol. PP, no. 99, pp. 1–1, 2017.
[25] Q. Xu, X. Hu, P. Wang, J. Xiao, P. Tu, C. Wen, and M. Y. Lee, "A decentralized dynamic power sharing strategy for hybrid energy storage system in autonomous dc microgrid," *IEEE Trans. Ind. Electron.*, vol. 64, no. 7, pp. 5930–5941, Jul. 2017.
[26] M. Hamzeh, A. Ghazanfari, Y. A. R. I. Mohamed, and Y. Karimi, "Modeling and design of an oscillatory current-sharing control strategy in dc microgrids," *IEEE Trans. Ind. Electron.*, vol. 62, no. 11, pp. 6647–6657, Nov. 2015.
[27] H. Mahmood, D. Michaelson, and J. Jiang, "A power management strategy for pv/battery hybrid systems in islanded microgrids," *IEEE Jour. Emerg. and Sel. Topics in Power Electron.*, vol. 2, no. 4, pp. 870–882, Dec. 2014.